Carrier-diffusion measurements in silicon with a Fourier-transient-grating method

Jan Linnros and Vytautas Grivickas*
Department of Electronics, Solid State Electronics Division, Royal Institute of Technology, Electrum 229, S-164 40 Kista, Stockholm, Sweden
(Received 15 November 1993; revised manuscript received 6 September 1994)

Carrier-diffusion measurements in silicon using a newly developed Fourier-transient-grating technique is presented. The method uses a laser light pulse projected through a semitransparent grid pattern to excite a sinusoidal excess carrier grating within the sample. The interdiffusion of carriers is monitored by free-carrier absorption of a focused infrared probe beam. The grating is scanned across the probe beam and the spatial Fourier transform is calculated at each sampling time following the excitation pulse. The resulting Fourier spectrum shows a peak for a frequency corresponding to the grating period and the decay of the amplitude of this spatial-frequency component represents a characteristic grating erasure time, which is related to the carrier diffusivity. This Fourier-transient-grating method allows sensitive measurements of the carrier diffusivity over a broad range of injection levels, both in the minority carrier regime as well as for high-injection conditions including the transition between the two regimes. Here, measurement data are presented for silicon samples of various doping concentration and types for excess carrier injections in the range $\sim 10^{12}$–10^{17} cm^{-3}. At low densities of injected carriers, our measurement data are in agreement with generally accepted low-injection lattice-scattering mobility values showing the transition to the high-injection range according to ambipolar theory. However, at excess carrier concentrations exceeding 10^{15} cm^{-3}, the diffusion coefficient is clearly reduced with respect to the ambipolar diffusivity (using constant electron and hole diffusivities) due to carrier-carrier scattering effects. This reduction is stronger above an injected carrier density of 10^{16} cm^{-3} than that predicted by many-body quantum theory [J. F. Young and H. M. van Driel, Phys. Rev. B **26**, 2147 (1982)]. The diffusivity data, converted to mobilities using Einstein's relation, have also been compared to recent semiempiric drift-mobility models used for semiconductor device simulation.

I. INTRODUCTION

Although the diffusion of charge carriers in semiconductors has been studied since the early stage of semiconductor research, most notably by the famous time-of-flight technique invented by Haynes and Shockley,[1] this subject remains relatively poorly investigated with respect to other semiconductor electrical properties. In particular, experimental data are lacking in the transition range between minority carrier diffusion and that of the ambipolar case.

The diffusion of charge carriers in semiconductors is traditionally related to the carrier mobility (μ) through[2,3]

$$D_i = \frac{F_{1/2}(\eta)}{F_{-1/2}(\eta)} \frac{kT}{q} \mu_i, \quad i = e,h \ , \tag{1}$$

where $F_{1/2}$ and $F_{-1/2}$ are the Fermi-Dirac integrals, and the index i stands for electron or hole diffusion/mobility. η equals $(E_F - E_c)/kT$ for electrons and $(E_V - E_F)/kT$ for holes, E_F, E_C, and E_V being the Fermi level, the conduction-band edge, and the valence-band edge, respectively. k, T, and q are the Boltzmann constant, the absolute temperature, and the elementary charge, respectively. For nondegenerate semiconductors Eq. (1) may be simplified to

$$D_i = \frac{kT}{q} \mu_i, \quad i = e,h \ , \tag{2}$$

which is commonly known as the Einstein relation. Equations (1) and (2) only relate the *majority*- carrier mobility to the corresponding diffusivity and, in a more general situation, such as during high injection conditions, the ambipolar diffusivity must be calculated from

$$D = \frac{n+p}{\frac{n}{D_h} + \frac{p}{D_e}} \ , \tag{3}$$

where D_e and D_h are the electron and hole diffusivities [which may be calculated using Eqs. (1) and (2)], respectively, and n and p are the electron and hole carrier concentrations. Physically, the ambipolar diffusivity arises from the fact that an electric field will develop due to the fast moving electrons with respect to the more slowly moving holes. This will tie electrons and holes together in a coupled diffusive motion.

For semiconductor devices, one of the most important aspects of the carrier diffusivity is the carrier-diffusion length given by

$$L = \sqrt{D\tau} \ , \tag{4}$$

where τ is the average carrier recombination lifetime. The diffusion length determines, for instance, the minority-carrier collection efficiency for a p-n junction (cf. solar cell, photo diode, etc.), and also several aspects of the operation of bipolar devices (power devices, etc.).

As the concentration of carriers or dopant atoms is in-

creased to very high densities (typically above 10^{19} cm^{-3} for $T \leq 300$ °C), degeneracy will occur and the carrier diffusion coefficient and the mobility are no longer linearly related.[2,3] In this region the diffusion coefficient, calculated from Eq. (1), increases steeply with carrier concentration, due mainly to an increase in the kinetic energy of the carriers.[4]

The mobility, describing the carrier drift velocity in an electric field, has been the subject of extensive modeling due to its prime importance for carrier transport in devices.[5–7] The main contributions to the mobility are (1) lattice scattering (2) impurity or defect scattering, and (3) carrier-carrier scattering effects. At room temperature, in very pure material and at low carrier concentrations, lattice scattering dominates whereas at high dopant concentrations, or during high carrier excitation conditions, the mobility is significantly reduced with respect to its maximum value. Accordingly, scattering against dopant atoms and scattering against the moving free carriers have been treated semiempirically by introducing appropriate scattering cross sections.[5,6]

Although the carrier diffusivity is commonly derived from the drift mobility using Einstein's relation [Eq. (2)], at least two anomalies exist. The first one relates to higher injection regimes where carrier-carrier collisions dominate against other scattering mechanisms (i.e., for $\tau_{cc} < \tau_i$, τ_l; τ_{cc}, τ_i, and τ_l being the mean time between scattering events for carrier-carrier, impurity, and lattice scattering, respectively). The main contribution to carrier-carrier scattering is via electron-hole (*e-h*) collisions. This involves a momentum transfer between the two particles, and results in a net momentum exchange between the two particle distributions. Collisions among electrons (*e-e*) or among holes (*h-h*), on the other hand, do not lead to an overall momentum change, as energy and momentum are conserved within the respective particle distributions. However, such collisions may serve to thermalize hot carriers and, thus, influence the scattering efficiency as a second-order effect due to the energy dependence of other scattering mechanisms (e.g., impurity scattering). Since in a drift situation electrons and holes are moving in opposite directions, frequent collisions involving momentum exchange will occur resulting in a considerable reduction of the drift mobility (and the corresponding current). In a diffusive situation, on the other hand, *e-h* scattering will be less efficient, and the diffusivity may not be calculated using measured drift mobilities.[8–10]

To account for these differences a mobility dependent on the *e-h* relative velocities (and direction) must be introduced, resulting in a coupling between the electron and hole transport currents.[7,11,12] As a consequence, an essentially constant diffusion mobility has been predicted at injections where the normal drift mobility is reduced due to *e-h* scattering.[7,8] The modified scattering cross sections, dependent on the *e-h* relative velocity, also result in the intriguing "drag effect" for the case of minority-carrier transport: Minority carriers are swept along the massive flow of majority carriers, resulting in a much reduced minority-carrier mobility (Refs. 13 and 14 with cited papers). (Theoretically, a negative mobility may even be possible under certain conditions.)

An alternative approach for direct carrier *diffusivity* calculations was suggested by Young and van Driel,[4] who introduced quantum calculations to treat "many-body" scattering effects. In these calculations the high density of carriers may be expressed as a dynamic narrowing of the band gap such that if a carrier density gradient is present it will be accompanied by a corresponding band-gap gradient that opposes the diffusive carrier flow and, thus, will lower the diffusivity. At this moment this is the most comprehensive theory for the injection dependence of the carrier diffusivity.

The second anomaly related to highly doped material ($n_0, p_0 > 10^{17}$ cm^{-3}) under minority-carrier injection, where the minority-carrier mobility for a given type (*p* or *n*) was shown to be higher than the corresponding majority-carrier mobility, i.e., *for the same type of carrier.*[15–17] Recent models attribute this effect to the screening of dopant atoms by the high density of majority carriers (see Refs. 6 and 18 and citations therein). Thus Eq. (2) cannot be used to obtain the minority-carrier diffusion length based on majority-carrier mobility data.

To resolve these anomalies and to provide accurate mobility/diffusivity data for device simulations, the carrier mobility and diffusivity must be mapped over a wide range of injection levels, for different doping densities, for *n*- and *p*-type materials, etc. Thus accurate carrier mobility and diffusivity measurement techniques are needed that allow independent variation of the carrier concentration (with respect to doping density) over several orders of magnitude. Furthermore, relatively homogeneous excitation conditions must be maintained, as several parameters depend critically on the injection level (e.g., bulk carrier lifetime, carrier mobility, surface recombination, etc.).

Traditional mobility measurement techniques are the Hall method, the time-of-flight technique, and various techniques to extract the mobility from devices [metal-oxide-semiconductor field-effect-transistor (MOSFET) mobility] etc; for a review, see Ref. 19. To obtain the carrier diffusivity (or the corresponding minority-carrier mobility), usually a photocurrent or a surface photo voltage is measured yielding the carrier-diffusion length.[15–17] To convert the diffusion length into a corresponding diffusivity, the carrier lifetime must be determined in an independent experiment. All these techniques have in common relatively extensive sample preparation procedures, and some of these methods have very limited applicability. Also, the derived mobility may not simply be taken as a true drift mobility (e.g., Hall mobility, MOSFET mobility). The holographic transient grating technique, on the other hand, was introduced as a direct method for carrier diffusivity determination.[20–23] The technique is based on the formation of an excess carrier grating by two interfering (pulsed) optical beams, which is detected by the (diffractive) deflection of either a third probe beam or by one of the interfering beams. Although limited to very high injections, this technique has served as a prototype for the method described below.

In a previous publication we presented a contactless method for carrier-diffusion measurements in silicon us-

ing an all-optical technique:[24] A carrier grating was created in the sample by projecting a grid of suitable dimensions using a laser pulse. The interdiffusion of carriers was monitored by detecting the transient free-carrier absorption with a second cw infrared laser finely focused to provide scanning across the carrier grating. By varying the contrast of the projection grid as well as the excitation beam intensity, the carrier injection level and the modulated carrier fraction (with respect to a homogeneously excited background) could be varied independently. The technique was demonstrated for a 1×10^{15} cm^{-3} p-type sample.

In the work presented here we have greatly improved the accuracy and sensitivity of the technique by introducing Fourier analysis of the measured carrier transients. Thus the diffusivity may be mapped with higher accuracy down to $\sim10^{12}$ carriers/cm^3. We demonstrate the method by mapping the diffusivity over five decades of injection levels for a variety of different samples. This allows a continuous transition from minority-carrier injection conditions to the high injection regime described by the ambipolar diffusivity. The resulting data are compared to diffusivities derived from models of the carrier mobility. We will further briefly outline how the technique can be generalized to provide simultaneous diffusivity and drift mobility measurements.

The paper is organized as follows. In Secs. II and III we present the experimental and mathematical background of the Fourier-transient grating (FTG) method, respectively. Section IV includes the diffusion measurement results of differently doped silicon specimens compared to theoretical or semiempiric mobility or diffusion models. A discussion is found in Sec. V, and a summary in Sec. VI.

II. EXPERIMENT

Measurements are performed with an all-optical, contactless pump-probe technique using the geometry shown in Fig. 1(a).[24] Excess carriers are generated by a short yttrium aluminum garnet (YAG) laser pulse and detected through free-carrier absorption of a continuous IR laser beam in perpendicular geometry with respect to the YAG beam.[25] Due to the relatively low absorption of the YAG beam (photon energy close to the band-gap energy of Si) and to beam expansion, a fairly uniform electron-hole plasma is created within the sample. The excess carrier grating is created by projecting the YAG pulse through a semitransparent sinusoidal-like grid pattern. By focusing the probe beam and aligning it within the sample to the projected grid, the corresponding excess carrier grating may be mapped by scanning either the probe beam or the grid in the X direction. To suppress detection noise and laser amplitude fluctuations, the measurements are performed in a repetitive manner using signal averaging.

A schematic layout of the main components in the setup is presented in Fig. 1(b). The YAG laser runs in the TEM_{00} mode (14-W max cw power) on $\lambda=1.06$ μm. Pulses of $\sim$250-ns duration are generated by acousto-optical Q switching at frequencies of $\sim$100 Hz and with

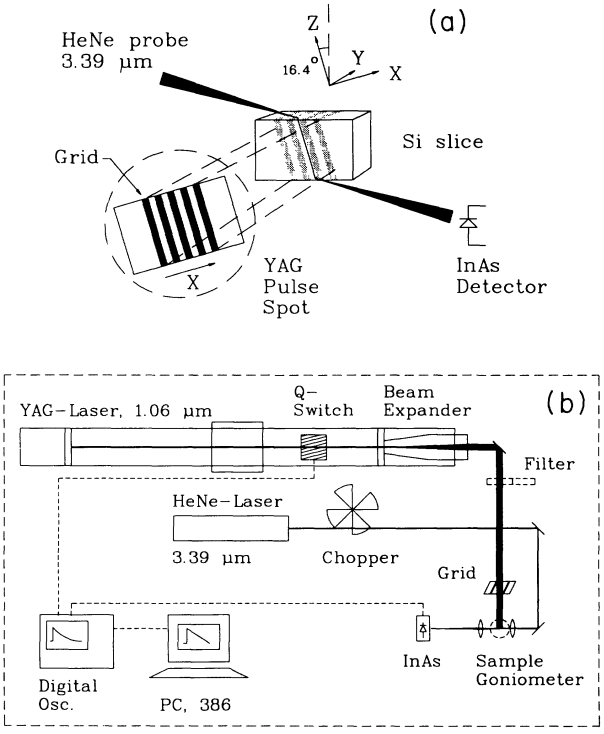

FIG. 1. Sample geometry (a), and a schematic of the experimental setup on the optical table (b).

typical pulse energies of a few mJ. A 1:10 beam expander provides a beam diameter of $\sim$4.5 mm (in some cases a larger expansion was used) at the sample, ensuring a relatively homogeneous excitation of the sample (without grid). Using a continuous neutral density filter (together with fixed damping filters, and by varying the laser current) the pulse energy is varied over a range of $\sim$5 decades.

A continuous wave (cw) HeNe laser at $\lambda=3.39$ μm (1 mW) is used for probing the excess carrier concentration within the sample. The beam is focused to an average diameter of typically $\sim$50 μm (depending on the sample size) within the sample, and enters and exits the sample through two parallel polished edges. By rotating the sample to allow Brewster's angle incidence, interference effects due to multiple reflections within the sample are largely suppressed. The transmitted beam is focused onto an InAs photovoltaic detector of 0.25-mm^2 area with a $\sim$10-ns rise time. The amplified signal is fed into a digital oscilloscope (175-MHz bandwidth, 100 M samples/s, eight-bit A/D conversion with 16-bit readout after averaging). After averaging 10^3–10^5 transients, depending on the injection level (to suppress noise), the decay data are transferred to a personal computer, where the measured absorption is converted to excess carrier concentration using a constant cross section σ_{eh} of 2.5×10^{-17} cm^2 (defined by $\Delta\alpha=\sigma_{eh}\,\Delta n,\Delta n=\Delta p$). This cross section was calibrated over a large range of injection levels by measuring the fraction of the incident YAG pulse energy that was absorbed in the sample (derived from measured incident, reflected, and transmitted pulse

TABLE I. Results from the fits of the electron and hole (low injection) diffusivities (D_e and D_h) to the experimental data using Eqs. (3) and (19) for the different samples (FZ, float zone; CZ, Czochralski; NTD, neutron transmutation doped). Corresponding mobilities from Einstein's relation [Eq. (2)] are also listed. p- and n-type dopants are boron and phosphorus, respectively.

Sample	Doping (cm^{-3})	D_e (cm^2/s)	D_h (cm^2/s)	μ_e ($cm^2/V\,s$)	μ_h ($cm^2/V\,s$)
CZ-Si p type	1×10^{15}	35±2	11.6±1.0	1350	450
CZ-Si p type	2×10^{14}	35±2	11.6±1.0	1350	450
CZ-Si n type	1×10^{15}	36±4	11.6±0.5	1390	450
FZ-Si p type	3×10^{12}	34±3	11.0±1.0	1310	420
NTD-Si n type	1×10^{13}	45±7	12.0±0.5	1740	460

energies). Assuming a one-to-one photon to electron-hole-pair generation rate, the carrier density could be calculated and subsequently compared to the corresponding peak absorption coefficient of the probe beam.[26]

Samples were cut from ~1–2-mm-thick, high-quality, Czochralski (CZ)- or float zone (FZ) grown wafers, doped with boron or phosphorus as shown in Table I. After cutting, two opposing edges were polished to optical quality using diamond paste. The sample alignment procedure started by reflecting a visible HeNe laser beam, collinear with the IR beam ($\lambda=3.39\ \mu m$), back from the polished entrance edge, i.e., perpendicular to the surface. The sample was subsequently rotated to the Brewster angle, i.e., 73.6° from the surface normal, followed by detector signal optimization by adjusting the detector position. Finally, the grid was aligned with the probe beam path within the sample, first by rough visual alignment, then by scanning the grid in the X direction [see Fig. 1(a)] and observing the excess carrier amplitude after the YAG pulse for various grid tilt angles. The tilt angle resulting in maximum amplitudal modulation across the grating was then selected as giving the best alignment.

III. FOURIER TRANSIENT GRATING METHOD

A. Carrier distribution resulting from homogeneous excitation

The distribution of carriers in a semiconductor sample resulting from a homogeneous (i.e., without a projected grid) optical excitation pulse is well known. For a short pulse duration compared to the characteristic time constants of the subsequent recombinative decay, the carrier distribution following the light flash is determined by the number of absorbed photons per unit area and depth within the sample:

$$\begin{aligned} n(x,y,z,t=0) &= \int g(x,y,z,t)\,dt \\ &= g_x(x)g_z(z)[k_1\exp(-\alpha y)+k_2\exp(\alpha y)]\delta(t)\ , \end{aligned} \tag{5}$$

where $g(x,y,z,t)$ is the optical generation rate of electron-hole pairs, and $\delta(t)$ is the delta function. For a coordinate centrum in the middle of the sample [with x, y, and z coordinates parallel to X, Y, and Z coordinates of Fig. 1(a)], k_1 and k_2 are given by

$$\begin{aligned} k_1 &= \frac{g_0\alpha(1-R)\exp(-\alpha d/2)}{1-R^2\exp(-2\alpha d)}\ , \\ k_2 &= k_1 R\exp(-\alpha d)\ , \end{aligned} \tag{6}$$

where α and R are the absorption and reflection coefficients, respectively, for the exciting photons, and $g_x(x)$ and $g_z(z)$ simple Gaussian-type photon distributions of the TEM_{00} mode.

The subsequent decay of the carrier distribution in the sample is due to carrier recombination in the semiconductor volume and at the sample surfaces and, after a certain time period, the system reattains the equilibrium state. The process of recombination and diffusive carrier redistribution can be mathematically described by solving the diffusion equation with a recombination term, characterized by the (bulk) carrier lifetime τ according to

$$\frac{\partial n(x,y,z,t)}{\partial t} = \frac{\partial}{\partial y}D\frac{\partial}{\partial y}n(x,y,z,t) - \frac{n(x,y,z,t)}{\tau}\ , \tag{7}$$

with boundary conditions of the type

$$\begin{aligned} D\frac{\partial n}{\partial y} &= s_1 n\ , \quad y=-d/2\ , \\ D\frac{\partial n}{\partial y} &= -s_2 n\ , \quad y=d/2\ , \end{aligned} \tag{8}$$

where s_1 and s_2 are the surface recombination velocities of the front and back surfaces, respectively, and with similar boundary conditions at the $x=-l/2$ and $l/2$ and the $z=-w/2$ and $w/2$ edges of the sample. At this point, we would like to note that, if higher-order recombination processes are not effective, and if the parameters D, s, and τ are slowly varying function of $n(x,y,z,t)$, the linearity of Eq. (7) allows variable separation and the solution can be written as

$$n(x,y,z,t)=n_x(x,t)n_z(z,t)n_y(y,t)\ . \tag{9}$$

For sample dimensions $d \ll w,l$, the problem can be treated in one dimension, with y of Fig. 1(a) being the main spatial variable and where the influence of the lateral dimensions (n_z,n_x) can be considered as small time varying perturbations to n_y.[27] That corresponds to a carrier depth distribution of the form

$$n_y(y,t)=\sum_{k=1}^{\infty} A_k\sin(a_k y)\exp\left[-\left[\frac{1}{\tau}+a_k^2 D\right]t\right]\ , \tag{10}$$

where τ is the recombinative time, a_k and A_k are surface-recombination-determined constants, and the summation is made for an infinite number of recombination modes, k. The full recombination process can be described mathematically in two phases; first, when the carrier diffusion process toward the surface is being established; and second, when a stationary flow of carriers is finally settled. In the second phase, a constant effective

lifetime is obtained throughout the sample. For samples of high surface recombination velocity ($2sd \gg \pi^2 D$) the effective lifetime τ is always smaller than the bulk lifetime τ_b, and is given by[27]

$$\tau^{-1}=\tau_b^{-1}+\pi^2 D\left[\frac{1}{d^2}+\frac{1}{w^2}+\frac{1}{l^2}\right] . \tag{11}$$

To illustrate the overall carrier depth dynamics within the sample, Fig. 2 shows depth profiles of the excess carrier density at various time durations following the excitation pulse (without grid) for a 1-mm-thick p-type sample. The profiles were obtained by taking averaged decays followed by stepwise scanning of the sample in the Y direction; see Fig. 1(a). From the curve at $\Delta t=1.0$ μs a slight depth variation of the excited carrier density is observed indicating an "effective" absorption coefficient of ~ 6.5 cm^{-1} [cf. Eqs. (5) and (6) for the "true" absorption coefficient] for the $\lambda=1.064$-μm light (incident at zero depth).[25] Even at this short-time interval, a reduction of the carrier concentration at the surfaces is clearly observed becoming more pronounced at later time intervals and, finally, sets the effective lifetime of the sample to ~ 50 μs. Notably, for excess carrier densities well above the doping level, 10^{15} cm^{-3} in this case, the high injection lifetime (τ_b) and the appropriate ambipolar diffusion coefficient D should be used [cf. Eq. (3)].

At this point, it is worth noting that Eq. (11) can be utilized to derive the carrier-diffusion coefficient from a lifetime measurement in the limit when a stationary carrier flow has been settled.[9,25,28] Similarly, Eq. (4) is often used to extract the diffusivity from the carrier flow toward a p-n junction. These methods, however, may contain a systematic uncertainty due to the highly nonhomogeneous carrier distribution in the sample which necessitates the use of averaged parameters for τ_b, s, and D, although these parameters are highly density dependent.

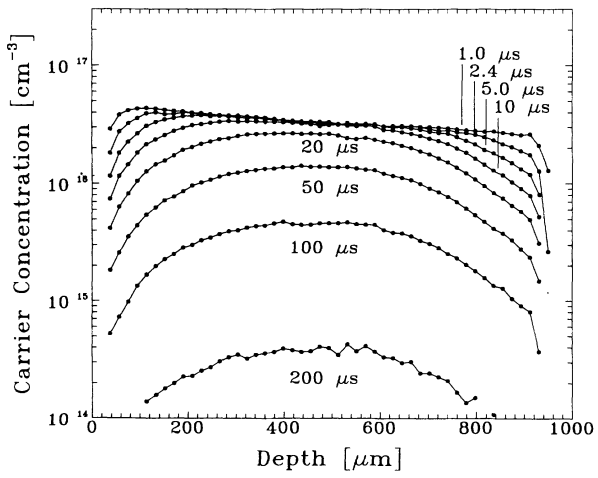

FIG. 2. Excess carrier depth profiles (without grating) in a 10^{15}-cm^{-3} doped, p-type sample for various times after the optical excitation pulse. The depth scale corresponds to the Y direction of Fig. 1(a) where the sample surfaces are located at 0 and 1000 μm.

B. Carrier distribution in a transient grating decay

For an excitation light pulse projected through a grid according to the geometry of Fig. 1(a), the carrier generation function in the x direction $g(x)$ is spatially modulated, and may be written as

$$g_x(x)=g_1 \sin(2\pi x/\Lambda+\phi)+g_2 , \tag{12}$$

where Λ is the period of the grid pattern, and ϕ is an arbitrary phase angle. The decay of the corresponding excess carrier grating has a term independent of the x coordinate (i.e., the average carrier concentration) $n_2(t)$, and a spatially varying term[20]

$$n_x(x,t)=n_2(t)\sin(2\pi x/\Lambda+\phi)+n_2(t) , \tag{13}$$

where $n_1(t)$ designates the time-varying modulation amplitude. Equation (13) represents the first terms in a Fourier expansion of $n_x(x,t)$. Higher spatial harmonics will be present if the generation function is not a pure sine function (with $2\pi/\Lambda_j=j2\pi/\Lambda$, with j an integral number); cf. Sec. III D. When the expression for $n_x(x,t)$ is inserted in an equation similar to Eq. (7) (diffusion in the x direction), exponential solutions for $n_1(t)$ and $n_2(t)$ are obtained:

$$\begin{aligned} n_1(t)&=n_1(0)\exp[-t/\tau_g] , \\ n_2(t)&=n_2(0)\exp[-t/\tau] , \end{aligned} \tag{14}$$

where τ_g is given by

$$\frac{1}{\tau_g}=\frac{1}{\tau}+\frac{4\pi^2 D}{\Lambda^2} . \tag{15}$$

Physically, the decay of the grating amplitude is driven by lateral carrier diffusion in the x direction, and the modulation will disappear in a characteristic "erasure" time τ_g. The average carrier density, represented by $n_2(t)$, decays with the time constant τ, normally given by Shockley-Reed-Hall recombination. For very high carrier concentrations, where Auger recombination may be important, the recombinative term in the diffusion equation [Eq. (7)] must be modified, and no analytical solution can be obtained. However, for sufficiently small grating periods, the erasure time may still be small compared to the recombinative time and a formula similar to Eq. (15) may be used.[21–23]

Although the carrier grating can be scanned in the x direction at any depth in the sample, it is obvious from Fig. 2 that scanning in the depth centrum ($y=0$) is preferable since the carrier depth distribution is relatively homogeneous around this position. At this position and for small time intervals after the excitation pulse, the recombination process is virtually unaffected by surface diffusion, and the carrier removal in the center of the sample is controlled mainly by the much longer bulk recombination time τ_b.

In Fig. 3 a three-dimensional representation of measured transient grating decays in the middle of the sample are presented (peak excitation density $\sim 2\times 10^{16}$ cm^{-2}). The YAG pulse arrives at $t=10$ μs at the sample and each decay, i.e., for a fixed grating position, is taken with

a sampling rate of 4 M samples/s. The data clearly illustrate the erasure of the imposed carrier grating resulting in a uniform excitation by the end of the displayed time period. The grid spacing Λ for the data shown is 806 μm, and the contrast M is about 80% as determined from the formula

$$M=[n_{\max}-n_{\min}]/n_{\max}\ , \tag{16}$$

where $n_{\max}$ and $n_{\min}$, respectively, are the peak and minimum excess carrier densities at the arrival time of the YAG pulse; cf. Fig. 3. The contrast M can be varied arbitrarily using projection grids of different densities, fabricated from negative transparent film. The grid is moved stepwise in a direction perpendicular to the probe beam [X direction, cf. Fig. 1(a)] using a computer-controlled motorized micrometer. We preferred moving the grid rather than scanning the probe beam along the same axis for two reasons: First, the probe beam will be fixed with respect to the YAG pulse spot, thereby always probing the center of the excited area. Second, variations in the surface quality could deflect the beam slightly or change the fraction of transmitted light, resulting in amplitude variations which could interfere with the measured transients.

Figure 4 shows carrier profiles from the data of Fig. 3 at various times Δt after the YAG excitation pulse. The indicated grating period, $\Lambda=806$ μm, is derived from a similar scan over some ten periods, yielding a measurement accuracy of the grating period well below 5%.

C. Fourier data analysis

The data displayed in Fig. 4 show that an almost ideally shaped sinusoidal excess carrier grating is created within the sample. The erasure time in this case is of the order 10 μs. In a previous paper[24] we used a maximum carrier decay, i.e., a decay taken at a grid position of maximum initial excitation, and a close by minimum decay to extract this time constant by simply forming another decay and taking the difference between these two decays. However, the disadvantage was that the created grating had to be ideally symmetric in order that no net flow of carriers would exist along the X direction.

In order to suppress nonsymmetric effects of the excess carrier grating and to improve the detection limit, we used a Fourier data analysis technique. In essence, the Fourier component related to the spatial frequency of the grid, i.e, proportional to Λ^{-1}, is calculated at every time data are sampled during the transient (of the form displayed in Fig. 3). By plotting the logarithm of the amplitude of this Fourier component with respect to time, an associated erasure time can be extracted from the slope. Thus nonsymmetric grating effects would be represented by other Fourier components and should, in principle, not affect the grating erasure time. As will be discussed below, the Fourier data analysis method is quite general and does not require a sinusoidal-shaped grating. With regard to sensitivity, we have been able to extend our detection limit to about one order of magnitude lower injected carrier density compared with our previous work.[24]

D. Fourier formalism and diffusivity determination

In brief, a periodic function $f(x)$ whose values are known on the points $x_k=2\pi k/N$, where $k=0,1,2,\ldots,N-1$, can be expanded in a Fourier series according to

$$f(x)=\sum_{j=0}^{N-1} c_j \exp(ijx)\ , \tag{17}$$

with complex i, and where the Fourier coefficients are

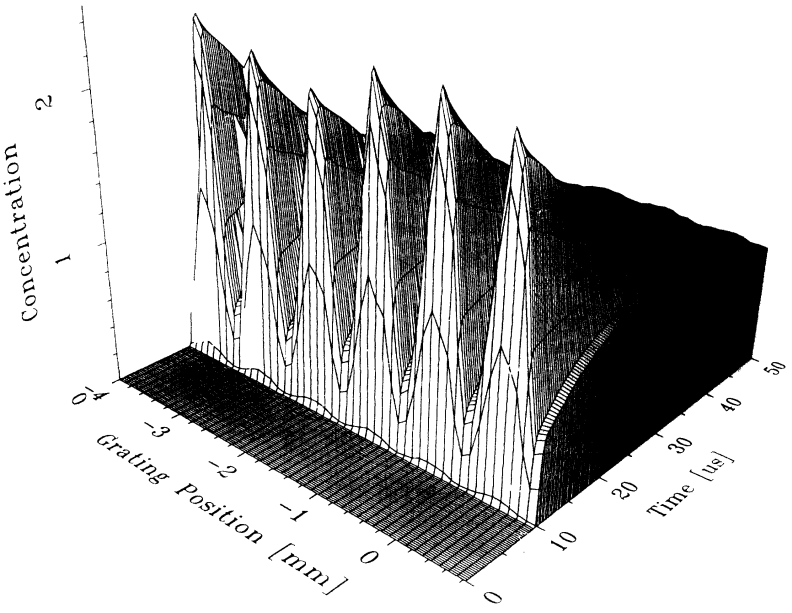

FIG. 3. Example of a transient grating measurement for a 10^{13}-cm^{-3}, n-type sample in the high injection regime (concentration scale: 10^{16} cm^{-3}). The data are shown as a 3D representation of decays (data at every 0.25 μs) taken at 49 grating positions.

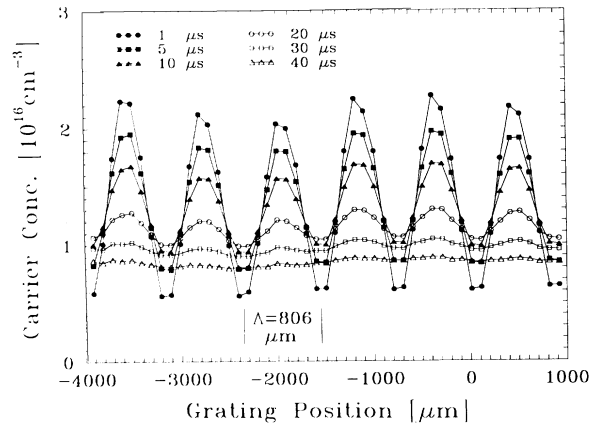

FIG. 4. Excess carrier concentration for a 10^{13}-cm^{-3}, n-type FZ sample as a function of the grating position along the X direction [cf. Fig. 1(a)] for various times after the optical excitation pulse. The grating period $\Lambda=806$ μm is indicated.

given by[29]

$$c_j=\frac{1}{N}\sum_{k=0}^{N-1} f\left[\frac{2\pi k}{N}\right]\exp\left[\frac{-ij2\pi k}{N}\right],$$

$$j=0,1,2,\ldots,N-1\ . \quad (18)$$

In our case a full set of transient data (see Fig. 3) (consisting of 49 decays, each of 200 carrier concentration values) is read into a computer program. The program has two modes of operation: A full Fourier calculation at a user-specified time or calculation of a few Fourier components c_j during the complete decay. These two modes are illustrated in Figs. 5 and 6, respectively. The computer code works according to Eq. (18), where $f(x)$ is treated as a function of only the grid position x for a *fixed* time.

Figure 5 shows calculated Fourier components at the time 12 μs (2 μs after the YAG pulse) for the data of Fig. 3. The component $j=0$, representing the average carrier concentration [cf. Eq. (18)], is not shown as it exceeds the vertical scale. Similarly, components 25–48 ($N=49$) are omitted as they represent negative spatial frequencies mirroring the first 0–24 components. The large peak for Fourier component No. 6 clearly represents the frequency corresponding to the six full periods of the grid on the measured x interval. By choosing an integral number of periods this peak will appear at a specific component number and its amplitude does not have to be interpolated, thus easing the interpretation of the calculated amplitude. In addition to the main peak some sidelobes may be seen and usually also a few overtones, typically for components 12, 18, and 24.

In Fig. 6 the calculated decay of component No. 6 is presented for three grating periods (the decay with $\Lambda=806$ μm calculated from the data of Fig. 3) measured on the same sample at approximately the same injection level. For $\Lambda=806$ μm the average of all decay data is also included (component No. 0), showing the simultaneous carrier recombination. Clearly, the grating erasure rate is much faster than the recombination rate, and the associated time constant depends quadratically on the grating period and can be calculated using Eq. (15). Conversely, the diffusivity can be derived from measurements of τ_g and τ. This is illustrated in Fig. 7, where grating erasure rates, i.e., τ_g^{-1}, are plotted versus Λ^{-2} for three grating periods calculated from the data of Fig. 6 (empty symbols, dashed line). Comparing with Eq. (15) yields a (ambipolar) diffusion coefficient $D\sim 14.5$ cm^{2}s^{-1}, and the offset corresponds to a recombinative lifetime $\tau\sim 120$ μs. This is in agreement with a lifetime calculated from the average concentration curve of Fig. 6 at a time of ~ 20 μs.

The procedure using different grating periods is tedious, due to the complicated grid alignment together with the combined measurement of Λ and the grating decays for each grating period. Instead, we have used Eq. (15) to calculate the diffusion coefficient directly. This requires a measurement of the recombinative lifetime (from the decay of component No. 0). Alternatively, the Fourier component decays may be normalized with respect to the decay of the average concentration, i.e., component No. 0. In this way the instantaneous lifetime τ is "subtracted" from the data, and τ_s^{-1} is directly proportional to D. The corresponding erasure rates using normalized Fourier amplitude decays (from a plot similar to that of Fig. 6) have also been plotted in Fig. 7, yielding $D=14.7$ cm^{2}s^{-1} (continuous line) with a negligible offset.

E. A generalized method including electric field

To further expand and generalize the Fourier treatment, in Fig. 8(a) we show the decays of component No. 6 and a few overtones, again calculated from the data of Fig. 3. Although, the overtone amplitude is more than an order of magnitude smaller than component No. 6, the initial fast decays (characterized by the decay constants τ_{gj}) can be used to construct a plot similar to Fig. 7 with Λ_j values corresponding to the overtone spatial periods;

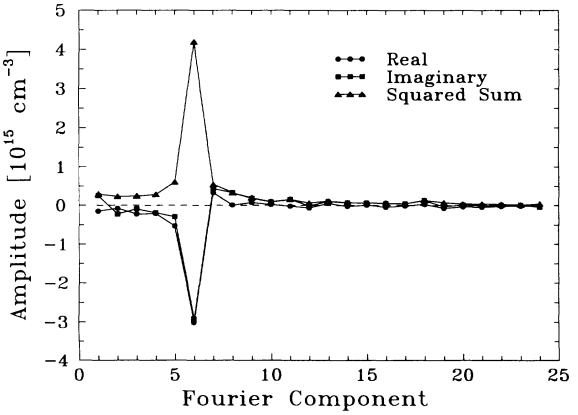

FIG. 5. Fourier component amplitudes at $t=2$ μs after the excitation pulse for a 10^{13}-cm^{-3}, n-type FZ sample. Component No. 0 (average carrier concentration along the grating) is not shown, as its amplitude exceeds the scale limits.

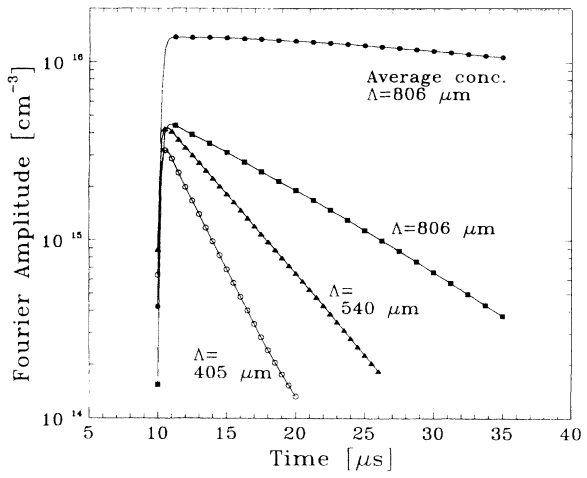

FIG. 6. The decay of Fourier component No. 6 using three different grating periods for a 10^{13}-cm^{-3}, n-type FZ sample. Also shown is component No. 0 for the largest grating period [cf. Fig. 4]. (For clarity only every fifth data point is represented by a symbol.)

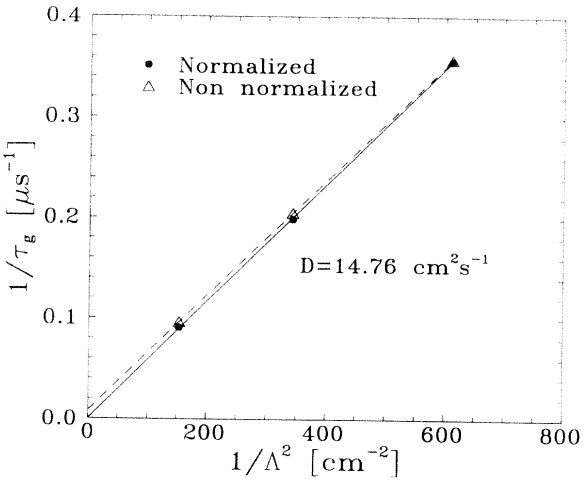

FIG. 7. Inverse grating erasure times vs $1/\Lambda^2$ for the three decays shown in Fig. 6 of the sixth Fourier component. The erasure times were derived from lines fitted to the decays over a selected time period, and in a normalized form where decays have been normalized to the decay of Fourier component No. 0 (see Fig. 6).

see Fig. 8(b). However, the relatively high noise levels for these overtones yield lower erasure rates, as evidenced by the Nos. 18 and 24 components.

The Fourier treatment is thus quite general, and does not require an ideal sinusoidal carrier excitation. In principle, one may therefore utilize any inhomogeneous carrier distribution to extract the diffusion coefficient. An example of a more "general" inhomogeneous carrier distribution would be the diffusional broadening of a point-like excess carrier excitation such as from a focused laser beam. The characteristic spatial frequency of the excited spot must, however, conform to the probe beam resolution and have a fast erasure time compared with the recombinative effective lifetime. The advantage with an excess carrier grating of the present type is the possibility to induce a small excess carrier modulation superimposed on a constant background (using a semitransparent grid). Thus the injection level can be kept essentially constant eliminating effects of differing diffusivity at the maxima and the minima of the excited grating (cf. Fig. 4 where, after 5 μs, the injection level varies less than a factor 2 across the grating).

As a further generalization of the technique one may also introduce an electric field along the grating (i.e., in the x direction). In the minority-carrier regime this introduces a parallel drift component that enables a simultaneous determination of the minority-carrier mobility similar to the Haynes-Shockley experiment[1] (cf. the time-of-flight technique[19]). The drift velocity is easily and very accurately calculated by the phase angle shift as a function of time for the Fourier component corresponding to the grating period. This was recently demonstrated in Ref. 30, where we also presented evidence of a minority-carrier drag effect (cf. Sec. I).

IV. CARRIER-DIFFUSION RESULTS

Experimental carrier diffusivity results plotted against the injected carrier density are summarized in Figs. 9 and 10. The diffusivities were derived using Eq. (15) in the normalized form (see Sec. III) from the erasure time of the main Fourier component (No. 6) of the decaying grating. In Fig. 9 data are presented according to doping type [Fig. 9(a) p type; Fig. 9(b) n type], whereas in Fig. 10 the same data are displayed according to material quality [Fig. 10(a) CZ-Si; Fig. 10(b) FZ-Si). The injection range is varied from 10^{12} to 10^{17} cm^{-3}. The dashed curves in Fig. 9 present two (ambipolar) diffusivity models, while the curves in Fig. 10 represent semiempiric drift mobility models[5,6] converted to diffusivity using Einstein's relation [Eq. (2)]. All theoretical calculations were performed using Eqs. (2) and (3), where n and p are the majority- or minority-carrier density of an extrinsic semiconductor according to

$$\begin{aligned} &n=n_0+\Delta n\ ,\quad p=p_0+\Delta p\approx\Delta p\quad (n\text{ type})\ ,\\ &p=p_0+\Delta p\ ,\quad n=n_0+\Delta n\approx\Delta n\quad (p\text{ type})\ . \end{aligned} \tag{19}$$

Since the recombination rate is very small during the time interval of the transient grating measurement, we may in all cases assume $\Delta n=\Delta p$, neglecting the influence of any trapped carriers.

The change of the diffusivity with injected carrier density in Fig. 9 clearly demonstrates two distinct regions: For low injection of excess carriers ($\Delta n<n_0$ or $\Delta n<p_0$ for n and p types, respectively) the diffusivity approaches a constant value characteristic of the minority carriers, i.e., that of electrons in p-type samples and that of holes in n-type samples. In the high injection case, on the other hand, it assumes a universal ambipolar dependence

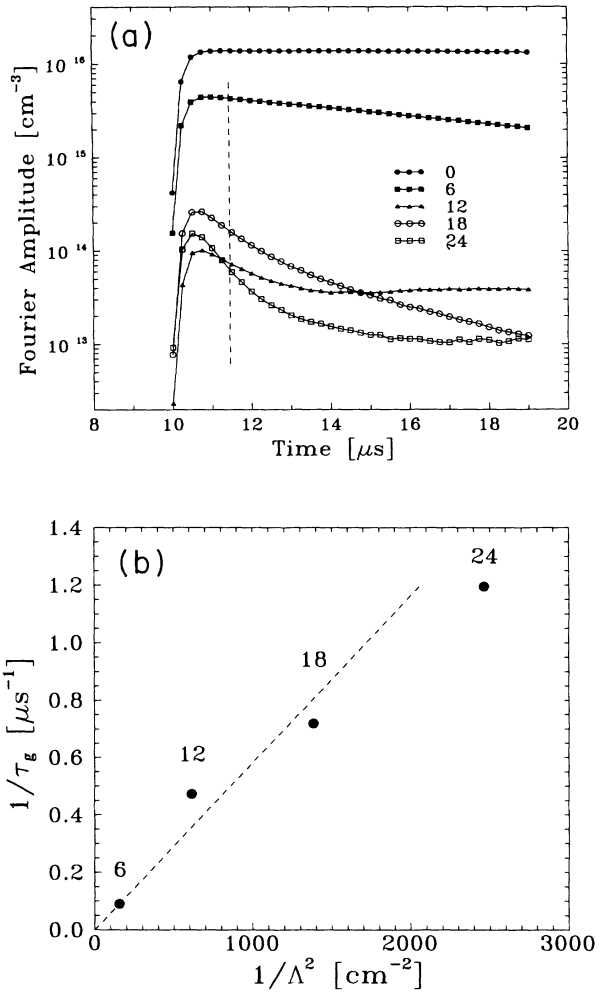

FIG. 8. The decay of the fundamental Fourier component No. 6 shown together with a few higher frequency multiples (a). The corresponding inverse decay constants, taken at the indicated line, are plotted in (b). The dashed line is *not* a fit to the data, but shows the line fitted to the data of Fig. 7 yielding $D=14.7$ cm^{2}s^{-1}.

($\Delta n > n_0, p_0$). As expected, the transition range depends critically on the relative injection level $\Delta n/n_0$ in an n-type sample and $\Delta n/p_0$ in a p-type sample.

At higher injections, typically $\Delta n > 10^{15}$ cm^{-3}, the experimentally determined diffusivities are reduced with respect to a constant ambipolar value. This is due to carrier-carrier scattering effects. At injections below $\Delta n = 1\times10^{15}$ cm^{-3}, however, this scattering is negligible, and D_h and D_e may be regarded as constants. That allows us to obtain pairs of D_h and D_e values applying the best fit of Eq. (3) (mainly restricted to the regime $\Delta n < 10^{15}$ cm^{-3}). The diffusion constants D_h and D_e and fitting errors are listed in Table I for each sample. The corresponding electron and hole (diffusion) mobilities according to Eq. (2) are also presented in the table for comparison. The best-fit curves are displayed in Fig. 9 as dashed lines. The data for the n-type samples [cf. Fig. 9(b)] yield a D_h of about 11.6 cm^2/s relatively accurately, while the electron diffusivity D_e is less accurate since the experimental data, for the measured injection levels, do not provide an asymptotic (minority-carrier injection) constant diffusivity [cf. Fig. 9(a)]. The fitted diffusivities using Eq. (3) for the p-type samples show that such an asymptotic electron-determined diffusivity can only be obtained for injections two orders of magnitude lower than the doping concentration. We may point out that in the fitting procedure slightly different combinations of the diffusion coefficients D_e and D_h also yield acceptable fits provided the ambipolar asymptote matches the data at higher injections.

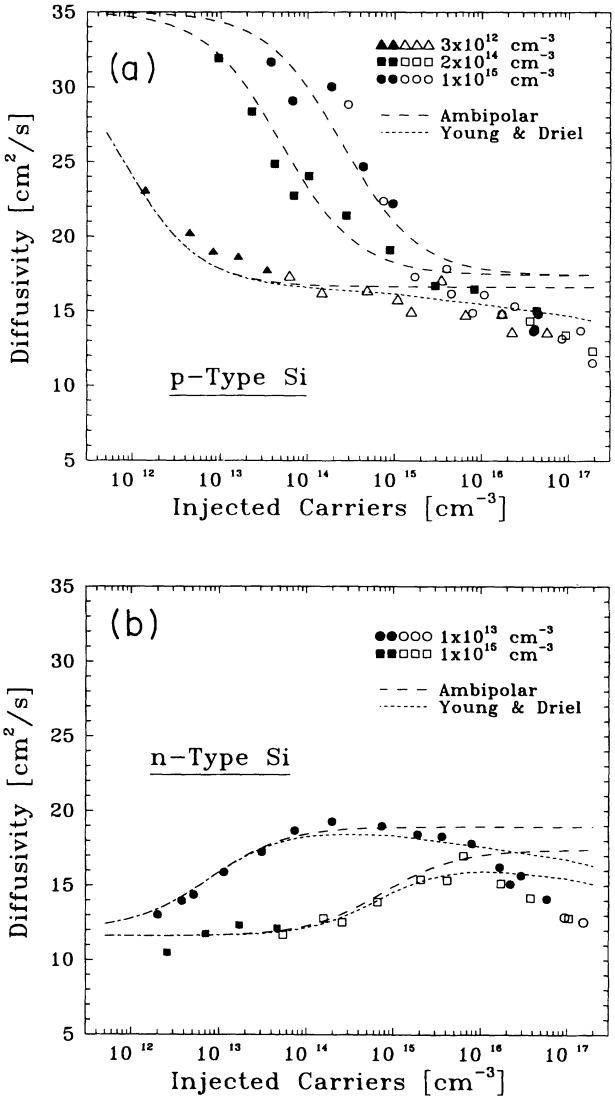

FIG. 9. Calculated carrier diffusivities using the Fourier-transient-grating method for (a) three p-type samples and (b) for two n-type samples. Filled symbols represent measurements using a grating period of $\Lambda=806$ μm, and open symbols those using a period of $\Lambda=540$ μm. Dashed lines indicate a theoretical ambipolar diffusivity [constant at high injections, cf. Eq. (3)] and a reduced ambipolar diffusivity, respectively, according to the theory of Young and van Driel (Ref. 4).

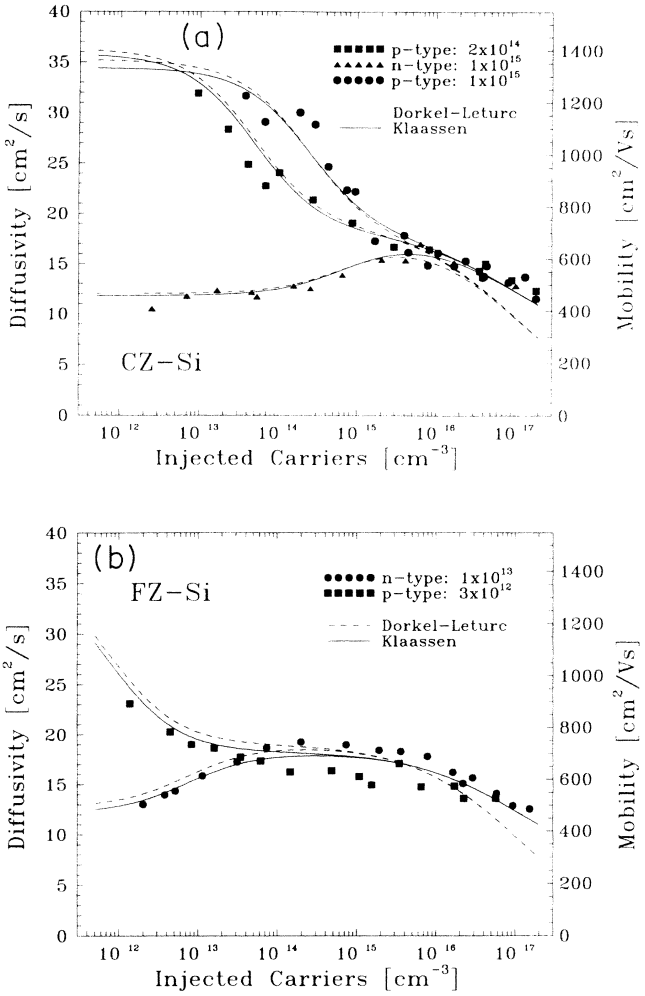

FIG. 10. Same experimental data as in Fig. 9, but sorted according to Si quality: (a) CZ-Si and (b) FZ-Si, respectively. The right-hand axis shows corresponding mobilities using Einstein's relation. Semiempirical theoretical models by Dorkel-Leturc (Ref. 5) and Klaassen (Ref. 6) are represented by dashed and full lines, respectively.

At this point we note that the derived minority-carrier diffusivities, converted to mobilities, correspond well to the generally accepted values for silicon. An exception is the extremely high electron diffusivity and mobility $D_e = 45$ cm^2/s resulting from the fit to the data for the float zone (FZ), NTD (neutron transmutation doped), 1×10^{13}-cm^{-3}-doped sample. (Indeed, if only injections below 5×10^{14} cm^{-3} are considered, an unphysically high $D_e = 58$ cm^2/s with $D_h = 11.6$ cm^2/s provides a better fit to the data.) This discrepancy is clearly evident in Fig. 10(b), where the two low-doped FZ samples (n and p types) yield quite different ambipolar diffusivities in the 10^{14}–10^{16}-cm^{-3} injection range.

In the high-injection range above 1×10^{15} cm^{-3}, however, the diffusion coefficient is no longer constant due to increasing carrier-carrier scattering. The theoretical predictions of many-body effects according to the theory of Young and van Driel[4] are included in Fig. 9 [for clarity only for the 3×10^{12}-cm^{-3}, p-type sample in Fig. 9(a)] by dotted lines. Although this theory correctly predicts the injection onset and the approximate size of the effect in the 10^{15}-cm^{-3} injection range, the measured reduction of the diffusivity is clearly stronger above an injection density of 10^{16} cm^{-3}. This has already been concluded from our preliminary results obtained by a simplified procedure in a 1×10^{15}-cm^{-3}-doped, p-Si CZ-grown sample.[24] In the present case (Figs. 9 and 10), it is clear that this effect is also independent of the sample doping and the sample type (in other terms, independent of the D_e and D_h low-injection values), at least for the moderate- and low-doped Si samples used in our investigations.

In Fig. 10 two semiempiric mobility models are shown for comparison; i.e., the Dorkel-Leturc model,[5] frequently used in device simulation codes, and a recent model by Klaassen.[6] For clarity, the diffusion mobility is called on the right-hand ordinate of Fig. 10 using the Einstein relationship [Eq. (2)]. Both models start at slightly different low-injection-determined mobilities, but treat carrier-carrier collisions in a different way. Therefore, both models have similar functional dependence at low-to-medium injections and seem to yield an approximate fit to the data. At high injections (above $\Delta n = 10^{16}$ cm^{-3}), however, the two models differ, and the Klaassen model seems to yield a better fit to the data.

Before discussing the data and the various theoretical diffusivity and mobility models, we would like to point out possible sources of systematic errors in our experimental data. These are related to (1) the calibration of the injected carrier density, Δn; (2) to the n_0,p_0 calibrated from the sample resistivity measurements; (3) to the erasure time τ_g measurement; and, finally (4) to the exact value of the grid period, Λ.

With respect to the conversion from the measured absorption to excess carrier density, we estimate the experimental uncertainty in our calibrated cross section ($\sigma_{eh} = 2.5\times10^{-17}$ cm^2) is better than $\pm20\%$,[26] although this procedure may also be affected by systematic errors (most likely less than $\pm50\%$). n_0 or p_0 are measured with a standard uncertainty of $\pm10\%$ in moderate-doped and $\pm20\%$ in low-doped samples. Note that $n_0(p_0)$ is quite important for obtaining the D_e and D_h values by the fitting procedure of Eqs. (3) and (19), in particular for our FZ-Si samples. As measured time constants, e.g., τ_g, are not affected by the absolute Δn calibration possible errors only result in a shift of the injection scale (cf. Figs. 9 and 10).

The typical uncertainty in the erasure time (τ_g) measurement is below $\pm10\%$. Thus we estimate a relative uncertainty in the diffusivity determination to be $\pm10\%$, although the scatter in the diffusivity data at medium-to-high injections is substantially lower. However, for low excess carrier densities the noise level in the Fourier amplitude is relatively larger (as in Fig. 6 type plots) introducing slightly larger errors in the erasure time determination.

As the period of the transient grating, Λ, is measured with an error of less than $\pm2\%$, this introduces an additional [cf. Eq. (15)] $<\pm5\%$ error in the diffusivity. This is further evidenced by the data for two different Λ periods, represented in Fig. 9 by filled and open symbols,

which show coincidence within ±5% error for the same injection level. Thus, in most cases, the absolute uncertainty in the diffusivity measurement we believe is about ±20%.

V. DISCUSSION

A. Low-injection range: $\Delta n < 10^{15}$ cm^{-3}

The presented low-injection diffusion and mobility values in Table I can be compared to the lattice scattering mobility values in silicon in the low impurity concentration limit:[6]

$$D_e = 36.8 \text{ cm}^2/\text{s}, \quad \mu_e = 1420 \text{ cm}^2/\text{V s},$$
$$D_h = 12.2 \text{ cm}^2/\text{s}, \quad \mu_h = 470 \text{ cm}^2/\text{V s}, \tag{20}$$
$$D_a = 2D_eD_h/(D_e+D_h) = 18.3 \text{ cm}^2/\text{s},$$

where D_a is the ambipolar diffusivity neglecting carrier-carrier scattering effects (maximum value for high injection). These parameters are equal to the highest experimentally obtained majority electron and hole drift mobilities at room temperature, and may equal the minority-carrier mobilities in pure material. However, for a shallow impurity concentration of $\sim 10^{15}$ cm^{-3}, the diffusion and mobility are reduced to the following values:[3-5,31]

$$D_e = 31.9 \text{ cm}^2/\text{s}, \quad \mu_e = 1230 \text{ cm}^2/\text{V s},$$
$$D_h = 11.7 \text{ cm}^2/\text{s}, \quad \mu_h = 450 \text{ cm}^2/\text{V s}, \tag{21}$$
$$D_a = 2D_eD_h/(D_e+D_h) = 17.1 \text{ cm}^2/\text{s}.$$

The data of Eqs. (20) and (21) agree with our values within the range of measurement error as summarized in Table I. The only exception is the electron value for the low-doped n-Si-FZ sample, the corresponding mobility of which is clearly higher than the generally accepted lattice mobility value for electrons. A low-temperature measurement should provide more clear interpretation of the diffusion and mobility in this case.

The difference between electron diffusivity in low doped p- and n-type FZ-grown samples may be explained assuming that the minority electrons in p-Si have lower mobility than the majority ones in n-Si. However, at high dopant concentrations (n_0 or $p_0 > 10^{17}$ cm^{-3}), it is now well established that the minority-carrier mobility is greater than the majority-carrier values.[6,16,32] This effect was attributed to less effective scattering by the ionized dopants because the scattering is repulsive for minority carriers but attractive for majority carriers.[6,33] We note that some experimental mobility data in the low doping range have been interpreted as the apparent difference between minority- and majority-carrier mobilities, i.e., by Susi *et al.*[31] (a higher minority-hole mobility with respect to the majority one). Recently Kay and Tang have shown theoretically that this effect is insignificant for dopant densities $\leq 10^{15}$ cm^{-3}.[18]

At low doping the role of e-h drag effects is theoretically expected at temperatures below 150 K,[13] and, hence, some differences in minority and majority-carrier mobilities could be expected in drift measurements. Some early data presented by Seeger[34] indeed showed lower minority-electron and minority-hole mobilities with respect to the majority ones.

The range of high doping and low temperatures is out of the scope of the present investigation. We think that the difference of our observed electron diffusion and mobility in FZ-Si samples, as shown in Fig. 10(b) and Table I, is not related to a difference in the minority- with respect to majority-carrier mobility. This conclusion is supported by the fact that we have not observed any difference in minority- and majority-carrier diffusion in higher-doped CZ samples [Fig. 10(a)]. As pointed in Sec. III E, the drift of carriers can also be investigated using our technique with an electrical field applied across the transient grating. The corresponding drift mobility can be extracted by Fourier phase-shift analysis. These measurements are in progress and the results were partly presented in Ref. 30.

B. High-injection range: $\Delta n > 10^{15}$ cm^{-3}

A reduction of the diffusivity due to carrier-carrier scattering in the injection range 10^{15}–10^{17} cm^{-3} is demonstrated by our data for different types of Si samples (Figs. 9 and 10).[35] The determined reduction is stronger than expected from first-principles analysis,[7,8,11] which predicts a nearly constant D_a value in this regime. Moreover, this reduction is stronger than that predicted by the many-body quantum theory calculation of Young and van Driel,[4] as evidenced from Fig. 9. This cannot be explained by thermal heating, since the effect has the same amplitude at different grating modulation rates[24] and since any heating produced by laser light in this range is estimated to be below 01. °C. Many-body quantum theory[4] predicts a maximum reduction factor at the injection range 10^{18} cm^{-3} to about $0.76D_a$ at room temperature. In classical calculations of the acoustic-phonon scattering, this factor was estimated to be slightly larger, i.e., about $0.88D_a$.[9,10,12] In both cases the direct dissipative effect due to e-h scattering is neglected. In a recent publication,[36] the effect of excitons on the diffusion was also calculated.

Our results are in agreement with the experimental values of $D = 7(\pm 3)$ cm^2/s at the injection $(1-4)\times 10^{18}$ cm^{-3} (Ref. 21) and $D = 8.3$ cm^2/s at 2×10^{19},[23] measured by the holographic transient grating technique. A similar value ($D = 7$ cm^2/s) was also measured in a diffusion-driven photodetector (transient grating moving in a small electrical field) at injections about 10^{18} cm^{-3} in low-doped silicon.[37] Recently, two techniques for the simultaneous measurement of the carrier lifetime and diffusion coefficient in silicon have been presented.[38,39] In the work by Rosling *et al.*[38] free-carrier absorption is used to measure the decay of an electrically excited p-i-n diode after switchoff, temporally as well as in depth. Their diffusivity data (in the injection range 2×10^{15}–3×10^{17} cm^{-3}) agree with our injection dependence behavior but are lower by a factor ~ 1.3.

By comparing our measured data with semiempirical models, as in Fig. 10, we attempt to show the expected diffusivities, derived from drift mobility data using the

Einstein relation, of commonly accepted simulation codes. The model by Klaassen[6] includes *e-h* scattering in the pure form, but neglects *e-e* and *h-h* collisions. The model by Dorkel-Leturq,[5] on the other hand, includes all kinds of carrier-carrier scattering but is based on earlier drift mobility data. However, both models predict a higher reduction of the diffusivity above the 10^{16}-cm^{-3} injection range, although the Klaassen model fits our data more closely. Thus we conclude that more precise theoretical calculations are needed for higher injections in order to elucidate carrier-carrier scattering effects on the carrier diffusivity.

VI. SUMMARY

A Fourier-transient-grating technique has been developed for the determination of carrier diffusivity with high precision over a large range of injection levels. The basic principle of the method is the formation of a spatially inhomogeneous excitation of carriers within the sample by projection of a laser pulse through a semitransparent pattern, such as a sinusoidal grid. The time and spatial dependence of the excess carriers is probed by free-carrier absorption of an infrared laser beam scanned across the inhomogeneous excess carrier plasma. By Fourier analysis (at each sampling time) the decay of selected spatial frequencies in the carrier plasma can be related to the carrier diffusivity. This improves considerably the sensitivity in terms of detected carrier density and, thus, the diffusivity determination for very low excess carrier concentrations. With this method we have characterized differently doped Si samples at injection ranging from $\sim 10^{12}$ to $\sim 10^{17}$ cm^{-3}. The resulting diffusivities compare well with semiempirical mobility models using the Einstein relation and drift mobility data up to injections of $\sim 10^{15}$ cm^{-3}. At higher injections carrier-carrier scattering effects reduce the diffusivity from a constant ambipolar value. This effect is larger than predicted by many-body quantum calculations, although the onset in terms of injected carrier density is correctly predicted by these calculations.

ACKNOWLEDGMENTS

The authors would like to acknowledge discussions with Professor E. Velmre, Dr. M. Rosling, and Dr. D. Noreika. Financial support was received from NUTEK. The work was mainly performed while the authors were with the Swedish Institute of Microelectronics.

---

*Permanent address: Semiconductor Physics Department and Institute of Applied Sciences, Vilnius University, 2054 Lithuania.

[1]J. R. Haynes and W. Shockley, Phys. Rev. **81**, 835 (1951).

[2]S. M. Sze, *Physics of Semiconductor Devices*, 2nd ed. (Wiley, New York, 1981), p. 29; R. A. Smith, *Semiconductors* (Cambridge University Press, Cambridge, 1959), Chap. 7; S. M. Ryvkin, *Photoelectric Effects in Semiconductors* (Consultants Bureau, New York, 1964), Chap. 13.

[3]A. P. Silard and M. J. Data, J. Appl. Phys. **62**, 3809 (1987).

[4]J. F. Young and H. M. van Driel, Phys. Rev. B **26**, 2147 (1982).

[5]J. M. Dorkel and Ph. Leturcq, Solid-State Electron. **24**, 821 (1981).

[6]D. B. M. Klaassen, Solid-State Electron. **35**, 953 (1992); **35**, 961 (1992).

[7]D. E. Kane and R. M. Swanson, J. Appl. Phys. **72**, 5294 (1992).

[8]Z. S. Gribnikov and V. I. Melnikov, Fiz. Tekh. Poloprovodn. **2**, 1352 (1968) [Sov. Phys. Semicond. **2**, 1133 (1969)].

[9]V. Grivickas, M. Willander, and J. Vaitkus, Solid-State Electron. **27**, 565 (1984).

[10]J. R. Meyer and F. J. Bartoli, Phys. Rev. Lett. **57**, 2568 (1986).

[11]E. Velmre, A. Koel, and F. Masszi, in *Proceedings of Simulation of Semiconductor Devices and Processes*, edited by S. Selberherr, H. Stippel, and E. Strasser (Springer-Verlag, Vienna, 1993), Vol. 5, p. 433, and references therein.

[12]D. E. Kane and R. M. Swanson, IEEE Trans. Electron Dev. **40**, 1496 (1993).

[13]M. Morohashi, N. Sawaki, and I. Akasaki, Jpn. J. Appl. Phys. **24**, 732 (1985).

[14]D. D. Tang, F. F. Fang, T. C. Chen, and G. Sai-Halasz, Int. Electron Devices Meet. Tech. Dig. 20 (1986); D. D. Tang, F. F. Fang, M. Scheuermann, and T. C. Chen, Appl. Phys. Lett. **49**, 1540 (1986).

[15]S. E. Swirhun, J. A. del Alamo, and R. M. Swanson, IEEE Electron Dev. Lett. **EDL-7**, 168 (1986).

[16]S. E. Swirhun, D. E. Kane, and R. M. Swanson, Int. Electron Devices Meet. Tech. Dig. 298 (1988).

[17]C. H. Wang, K. Misiakos, and A. Neugroschel, Appl. Phys. Lett. **57**, 159 (1990); **54**, 2233 (1989).

[18]L. E. Kay and T. W. Tang, J. Appl. Phys. **70**, 1475 (1991).

[19]D. K. Schroder, *Semiconductor Material and Device Characterization* (Wiley, New York, 1990), p. 194.

[20]K. Jarashiunas and J. Vaitkus, Phys. Status Solidi A **44**, 793 (1977).

[21]H. J. Eichler, F. Massmann, E. Biselli, K. Richter, M. Glotz, L. Konetzke, and X. Yang, Phys. Rev. B **36**, 3247 (1987).

[22]V. Grivickas, M. Willander, D. Noreika, M. Petrauskas, J. Knall, and W.-X. Ni, Semicond. Sci. Technol. **3**, 1116 (1988).

[23]V. Grivickas, V. Netiksis, D. Noreika, M. Petrauskas, M. Willander, M.-A. Hasan, and W.-X. Ni, J. Appl. Phys. **68**, 617 (1990).

[24]V. Grivickas and J. Linnros, Appl. Phys. Lett. **59**, 72 (1991).

[25]V. Grivickas, J. Linnros, A. Vigelis, J. Seckus, and J. A. Tellefsen, Solid-State Electron. **35**, 299 (1992).

[26]J. Linnros and M. Rosling (unpublished).

[27]J. McKelvey and R. Longini, J. Appl. Phys. **25**, 634 (1954).

[28]M. Kunst and A. Sanders, Semicond. Sci. Technol. **7**, 51 (1992).

[29]See, for instance, W. H. Press, S. A. Teukolsky, B. P. Flannery, and W. T. Vetterling, *Numerical Recipes* (Cambridge University Press, Cambridge, 1986), p. 381.

[30]J. Linnros and V. Grivickas, in *Physics of Semiconductors—Proceedings of the XXII International Conference*, edited by

D. J. Lockwood (World Scientific, Singapore, 1995).
[31]E. Susi, L. Passari, M. Merli, and M. C. Carotta, Phys. Status Solidi A **106**, 583 (1988).
[32]J. Dziewior and D. Silber, Appl. Phys. Lett. **35**, 170 (1979).
[33]A. B. Sproul, M. A. Green, and A. W. Stephens, J. Appl. Phys. **72**, 4161 (1992).
[34]K. Seeger, *Semiconductor Physics* (Springer-Verlag, Wien, 1973), Chap. 5.2.
[35]More precise measurements for injection ranges above 1×10^{17} cm^{-3} are also possible by the present Fourier transient grating technique, if thin Si samples and short laser pulses are used [V. Grivickas, D. Noreika, and J. Linnros (unpublished)].
[36]D. E. Kane and R. M. Swanson, J. Appl. Phys. **73**, 1193 (1993).
[37]A. Kostenbauder Appl. Phys. Lett. **51**, 1129 (1987).
[38]M. Rosling, H. Bleichner, M. Lundqvist, and E. Nordlander, Solid-State Electron. **35**, 1223 (1992).
[39]A. L. Filatov, V. I. Mirgorodsky, and V. A. Sablikov, Semicond. Sci. Technol. **8**, 694 (1993).

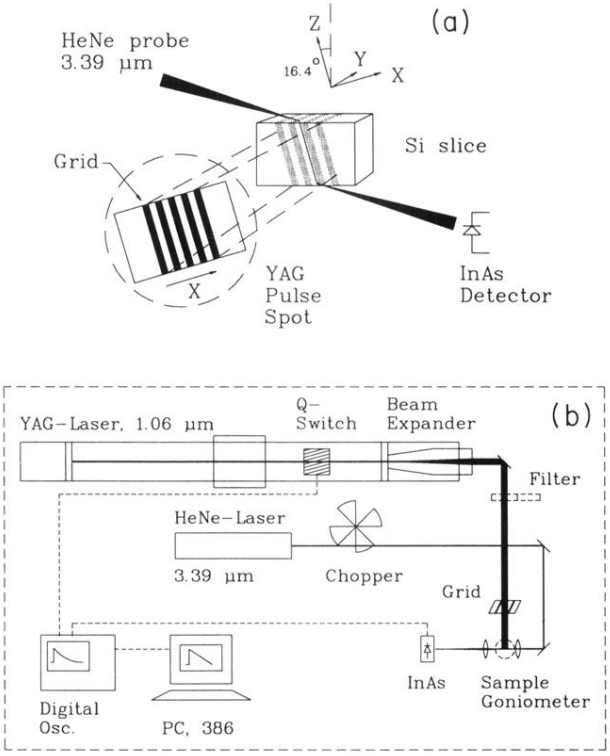

FIG. 1. Sample geometry (a), and a schematic of the experimental setup on the optical table (b).

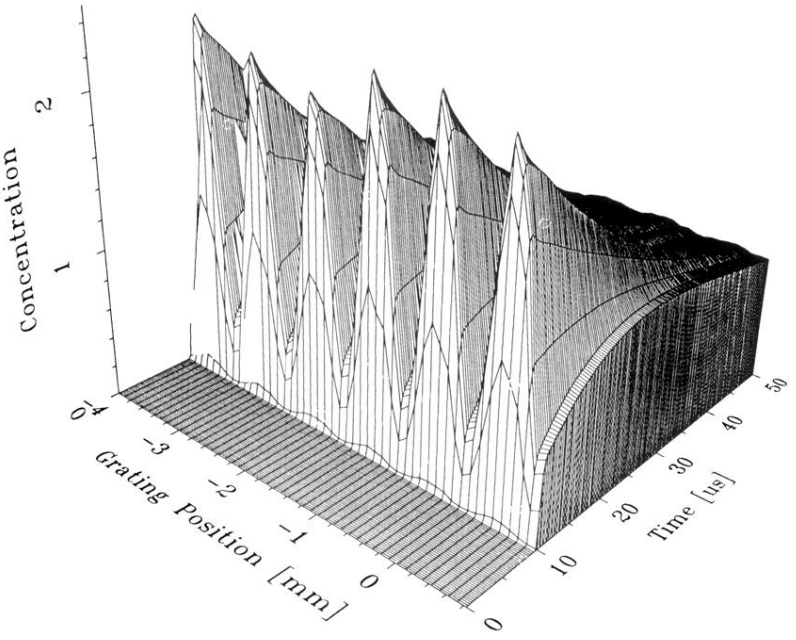

FIG. 3. Example of a transient grating measurement for a 10^{13}-cm^{-3}, *n*-type sample in the high injection regime (concentration scale: 10^{16} cm^{-3}). The data are shown as a 3D representation of decays (data at every 0.25 μs) taken at 49 grating positions.